MULTI-SPRING JOINT MODEL FOR INELASTIC BEHAVIOR OF STEEL MEMBERS WITH LOCAL BUCKLING

by

Ken-ichi OHI(I), Koichi TAKANASHI(II), and Ling-hua MENG(III)

1. INTRODUCTION

To establish the ultimate safety of structures to earthquake loading, often a huge number of numerical response simulation need to be carried out under an extensive set of earthquake motions considering various structural parameters. Analytical models of structures for such simulation are better to be simplified as much as possible but should not neglect essential natures of structural behaviors over elastic and inelastic ranges. Especially for steel frames, such as yielding, strain-hardening, Bauschinger's effect, local buckling, $P-\Delta$ effect, and so on, should be considered appropriately in the model construction.

In this paper, an analytical model termed 'multi-spring joint' is presented for the inelastic behaviors of steel members subject to uni-axial bending and axial loading. Similar modeling was proposed by Lai [1] for concrete members subject to bi-axial bending. Additionally, a hysteresis rule suitable to deal with inelastic cyclic behaviors of steel members including local buckling is proposed. After model parameters are calibrated to match with the results of the monotonic loading tests, which were carried out on H-shaped members with various width-to-thickness ratios, the validity of the model when it is used in the response analysis is checked through the comparison with the results of on-line response tests under earthquake loading.

2. MULTI-SPRING JOINT MODEL

It is assumed that a steel beam-column member can be divided into two kinds of portions as shown in Fig. 1: one is an elastic beam member and others are multi-spring inelastic joints. The member stiffness matrix for the elastic beam member can be derived on the basis of the infinitesimal deformation. Geometrical non-linearity is considered only for the displaced nodal positions at each stage in the incremental analysis to trace the equilibrium of a whole structure, while the secondary effects due to internal member deformation are ignored.

The length of the multi-spring joint denoted by L_j is assumed to be constant at each stage in the analysis, and its appropriate length depends on the size of the inelastic zone anticipated in each problem. The force and displacement vectors at the joint ends are defined as:

$$\{f\} = (f_{xi}, f_{yi}, m_i, f_{xj}, f_{yj}, m_j)^T \quad (1)$$

$$\{d\} = (d_{xi}, d_{yi}, \theta_i, d_{xj}, d_{yj}, \theta_j)^T \quad (2)$$

where the components of these vectors are defined in Fig. 2.

(I) Associate Professor, Institute of Industrial Science, Univ. of Tokyo
(II) Professor, ditto, (III) Graduate Student, Univ. of Tokyo

The multi-spring joint consists of four bar-springs and a shear panel. Each bar-spring is located in parallel at the distance of r_k from the center axis and connected to the both ends of the joint. Each bar-spring may carry axial force varying along its length as shown in Fig. 3, and the value at the middle point is chosen to represent the magnitude of the axial force in each bar-spring. Internal force and deformation vectors in the joint are defined as:

$$\{p\} = (p_1,\ p_2,\ p_3,\ p_4,\ q)^T \tag{3}$$

$$\{\delta\} = (\delta_1,\ \delta_2,\ \delta_3,\ \delta_4,\ \gamma)^T \tag{4}$$

where p_k: axial force carried by the k-th bar-spring at its middle point
q : shear force carried by shear panel
δ_k: axial deformation of the k-th bar-spring
γ : shear deformation of shear panel

The equilibrium equation and the compatibility equation for the joint are written as:

$$\{f\} = [C]\{p\} \tag{5}$$

$$\{\delta\} = [C]^T\{d\} \tag{6}$$

where [C] is the connectivity matrix between the joint-end forces and the internal forces in the joint:

$$[C] = \begin{bmatrix} -1 & -1 & -1 & -1 & 0 \\ 0 & 0 & 0 & 0 & 1 \\ r_1 & r_2 & r_3 & r_4 & 0.5L_J \\ 1 & 1 & 1 & 1 & 0 \\ 0 & 0 & 0 & 0 & -1 \\ -r_1 & -r_2 & -r_3 & -r_4 & -0.5L_J \end{bmatrix} \tag{7}$$

The relation between the force and displacement increments at the joint ends is written as:

$$\{\Delta f\} = [C][k^*][C]^T\{\Delta d\} \tag{8}$$

where [k*] is a diagonal stiffness matrix. Tangent stiffness of each bar-spring or shear panel is assigned to the diagonal element in this matrix. Such tangent stiffness is determined in accordance with the hysteresis rule, which is described in Section 3.

3. HYSTERESIS RULE FOR INELASTIC SPRING

(i) Skeleton Curves

Different skeleton curves are assigned to the tension side and the compression side behaviors of each bar-spring, respectively. The tension-side skeleton curve can be modeled so that its shape becomes similar to the uni-axial stress-strain curve of steel material. The compression-side skeleton curve shall be modeled so that it includes a negative-slope portion due to local buckling failure.

A piecewise-linear curve is used herein for the both side skeleton curves as shown in Fig. 4(a). The tension-side skeleton curve is composed of three lines, (1) elastic range, (2t) strain-hardening range and (3t) tensile strength level. The compression-side skeleton curve is also composed of three lines, (1) elastic range, (2c) strain-hardening range, and (3c) negative-slope range. In the case of a non-compact section fragile to local buckling, the strain-hardening range in the compression side might be omitted.

(ii) Shift of Skeleton Curves

Two points termed 'target points' on the skeleton curves, one for each side, are introduced herein. These points are referred to determine the curve shapes during cyclic reversals. The elastic-limit points on each side of the skeleton curve is assigned to each target point as the initial state.

When loading beyond the elastic-limit is made along one side skeleton with a certain amount of plastic deformation, the target point in the loading side moves together with the loading point, and at the same time, the other side skeleton curve shall be shifted to the loading direction as much as Ψ times the plastic deformation. Such a loading procedure on the skeleton curve is illustrated in Fig. 4(b). If zero is assigned to Ψ, neither hardening nor degrading would occur during cyclic reversals within the past peak amplitude. If one is assigned to Ψ, the hysterisis curve includes no softened portion due to Bauschinger's effect. Actual behaviors of inelastic portions in steel members are believed to fall on the intermediate state between these two extreme states.

(iii) Unloading Path

Unloading path is modeled as shown in Fig. 4(c) so that the curve becomes a portion of the Ramberg-Osgood function, $\delta = R_O(p)$. The parameters included in this function is determined to satisfy the following conditions:

$$\delta_U = R_O(p_U) \tag{9}$$

where the point on the curve, (δ_U, p_U), is the starting point of unloading. This is not always a point on the skeleton curve. When the unloading occurs at any time during cyclic reversals, this point shall be substituted by the last turning point.

$$\delta_T = R_O(p_T) \tag{10}$$

where the point, (δ_T, p_T), is the target point on the skeleton curve in the unloading direction.

$$k_E \cdot \frac{dR_o}{dp}\bigg|_{p=p_U} = 1 \tag{11}$$

where k_E is the initial unloading stiffness. The initial elastic stiffness is assigned herein to k_E.

The curve in the unloading path is determined from Eqs. (9), (10) and (11), and the tangent stiffness, k^*, on the curve is given by the following function in terms of the present restoring force:

$$k^* = \frac{k_E k_A}{k_A + r(k_E - k_A)\left|\dfrac{p - p_U}{p_T - p_U}\right|^{r-1}} \tag{12}$$

where $$k_A = \frac{p_T - p_U}{\delta_T - \delta_U} \tag{13}$$

4. RESPONSE ANALYSIS PROCEDURE

In a strict sense, the diagonal element, k*, of the stiffness matrix shown in Eq. (8) shall not be the tangent stiffness in the state before the incremental loading is posed, but the secant stiffness during the incremental loading. An iterative technique is needed, however, to evaluate such secant stiffness which depends on the amount of increment to be posed. In this paper, the stiffness is approximated by the tangent stiffness in the pre-increment state. The equilibrium error induced by such approximation is monitored and corrected at every time step in the following procedure. Similar technique is being used in some of the existing program codes for inelastic response analysis of frames [2].

(i) All the tangent stiffness matrices of the members and the joints are gathered, transformed with reference to the present nodal positions, and superposed into the following tangent stiffness matrix for the whole structural system:

$$\begin{Bmatrix} \Delta F_x \\ \Delta F_\theta \end{Bmatrix} = \begin{bmatrix} K_{xx} & K_{x\theta} \\ K_{\theta x} & K_{\theta\theta} \end{bmatrix} \begin{Bmatrix} \Delta x \\ \Delta \theta \end{Bmatrix} \tag{14}$$

where F_x, x: force and displacement vectors associated with inertial mass, respectively. These terms appear in the condensed equation of motion.

F_θ, θ: force and displacement vectors associated with static force constraints, respectively. These terms can be eliminated from the condensed equation of motion.

(ii) The condensed equation of motion is numerically integrated by using the central finite difference method, and the increment of the mass-associated displacement vector is written in the case of no damping as:

$$\{\Delta x\}_{(i \to i+1)} = \{\Delta x\}_{(i-1 \to i)} - \Delta t^2 \{[M]^{-1}\{F_x\}_{(i)} + \ddot{y}_{(i)}\{1\}\} \tag{15}$$

(iii) The increment of the force-constraint displacement vector is obtained from the mass-associated displacement vector as follows:

$$\{\Delta\theta\}_{(i \to i+1)} = [K_{\theta\theta}]_{(i)}^{-1} [\{\{F_\theta\}_{(0)} - \{F_\theta\}_{(i)}\} - [K_{\theta x}]_{(i)}\{\Delta x\}_{(i \to i+1)}] \tag{16}$$

where the term $\{F_\theta\}_{(0)} - \{F_\theta\}_{(i)}$ is the equilibrium error monitored at the i-th step. By using this scheme, the equilibrium unbalance would disappear at the next step, provided that the tangent stiffness matrices $[K_{\theta\theta}]_{(i)}$ and $[K_{\theta x}]_{(i)}$ are valid for the following time increment.

(iv) The incremental joint-end displacement are transformed from $\{\Delta x\}_{(i \to i+1)}$ and $\{\Delta\theta\}_{(i \to i+1)}$ through the transform matrix $[T]_{(i)}$ based on the last nodal positions at the i-th step. The internal displacement incre-

ment in the joint, $\{\Delta\delta\}_{(i\to i+1)}$, is obtained straightforwardly by Eq. (6).

(v) The restoring force vector of the springs, $\{p\}_{(i+1)}$, is obtained by tracing the hysteresis rule proposed in Section 3.

(vi) The joint-end force vector, $\{f\}_{(i+1)}$, can be obtained from $\{p\}_{(i+1)}$ by using Eq. (5). The nodal force vectors, $\{F_x\}_{(i+1)}$ and $\{F_\theta\}_{(i+1)}$, can be transformed from all the member-end and the joint-end forces through the transform matrix, $[T]_{(i+1)}$, based on the newly displaced nodal positions at the (i+1)-th step.

5. MONOTONIC LOADING TESTS

Monotonic bending tests were carried out on welded H-shaped members under constant axial loads. Stress-strain curve of material, cross sections used, and test setup are shown in Figs. 5 to 7, respectively. Three kinds of member section were welded from steel plates, which are made of the low-yield-ratio high-strength steel recently developed in Japan. The flange width-to-thickness ratios are 6, 8, and 10. Constant axial loads were applied to the specimens as much as zero, 20, 40, or 60 percent of their yield axial loads.

The parameters included in the multi-spring model and the hysteresis rule are arranged in the following manner:

(1) Each flanges and each half webs are idealized as lumped area bars shown in Fig. 6. The location of the bars is determined so that both the plastic modulus and the moment of inertia of the 4-point cross-section remain the same as the original ones.
(2) For the tension side skeleton curve, the yield stress and the tensile strength of each bars are derived from the results of tension tests on flange coupons. The slope of the strain-hardening portion is determined so that the line shares a single point with the observed stress-strain curve as shown in Fig. 5.
(3) For the compression side skeleton curve, the yield stress and the strain-hardening slope are assumed to be the same with the tension-side ones. The maximum resistance and the negative slope are arranged through calibration with the bending test results, but they are assumed to have the common value for the same flange width-to-thickness ratio.
(4) No shifting of the tension-side skeleton curve is made only in the case that the loading is made along the negative-slope skeleton in the compression side. Otherwise, the parameter for shifting the opposite-side skeleton curve, Ψ , is assumed to be 0.5. The parameter of the Ramberg-Osgood function, r, is set to 5.
(5) The shear panel is assumed to remain elastic.

The load-deflection curves observed in the monotonic loading tests are shown in Figs. 9(a) to (c) and compared with the model curves based on the multi-spring joint model arranged in the above-mentioned manner. It should be noted that the negative slope in these curves includes the $P-\Delta$ effect as well as the resistance deterioration due to local buckling failure. The model curves do not agree with the test curves in all the details, but the global behaviors observed in the tests can be traced by these simplified models.

6. COMPARISON WITH ON-LINE TEST RESULTS

On-line tests were carried out by using the same test setup on the same specimens as the monotonic loading tests mentioned in Section 5. Analyzed single-degree-of-freedom vibrational system is illustrated in Fig. 8(b), where the fictituous mass is arranged so that the natural period in elastic range becomes 0.8 seconds commonly. The N-S component recorded at El Centro in 1940 was used as excitation. Its peak acceleration was scaled to 1.2 and 1.6 times the yield acceleration of the analyzed structure. For the former case of input intensity, $\alpha_Y=1.2$, two conditions about axial load were considered, no axial load and 40 percent of yield axial load. For the latter case, $\alpha_Y=1.6$, only the condition with 40 percent of yield axial load was considered.

Response analysis was also carried out by using the multi-spring joint model arranged in Section 5. Hysteresis loops observed in the on-line tests and the model analysis are compared in Figs. 10 to 12. Response quantities, such as peak displacement, displacement range, and energy absorption, are compared in Figs. 13(a) to 13(c). The model analysis does not always follow exactly the displacement history observed in the on-line test. For example, the computed direction in which major permanent set occurs is sometimes opposite to the test result. It is seen, however, that the global damage levels and the response quantities compared in Figs. 13(a) to 13(c) can be well simulated by the present model.

7. CONCLUDING REMARKS

(i) The inelastic portion of steel beam-column member is modeled as a simple mechanism composed of inelastic bar-springs and a shear panel. A hysteresis rule for the bar-springs in such a multi-spring joint model is proposed to consider Bauschinger's effect under cyclic reversals as well as the resistance deterioration due to local buckling failure.

(ii) The parameters of the multi-spring joint model were calibrated to the results of monotonic loading tests, which were carried out on H-shaped beam-columns with various width-to-thickness ratios. Then the response analysis based on the model was carried out and compared with the results of on-line earthquake response tests. It is found that the global responses such as peak displacement, displacement range, and energy absorption are well predicted by the present model until the structure reaches to the final state in which the lateral resistance almost disappears.

REFERENCES

[1] Lai, S.S., Will, G.T. and Otani, S.:"Model for Inelastic Bi-axial Bending of Concrete Members,"ASCE, Vol.110, ST11, 1984.
[2] Kannan, A.E. and Powell, G.H.: "A General Purpose Computer Program for Dynamic Analysis of Inelastic Plane Structures with User's Guide," Report No. EERC 73-6 and 73-22, EERC, UCB, April 1973.

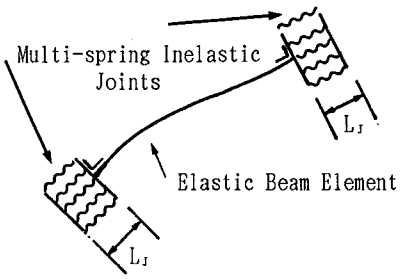

Fig. 1 Modeling of Steel Member

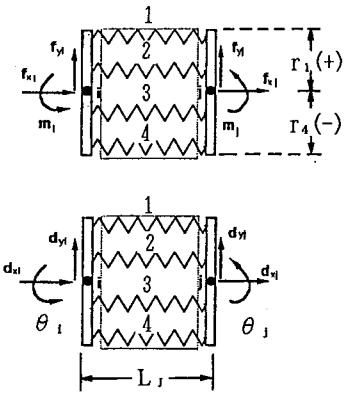

Fig. 2 Forces and Displacements at Joint Ends

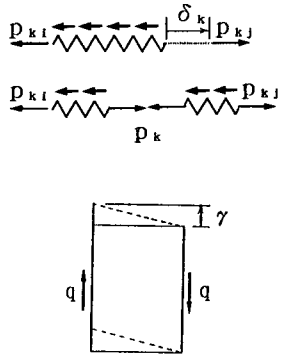

Fig. 3 Internal Forces and Deformation of Bar-springs and Shear Panel

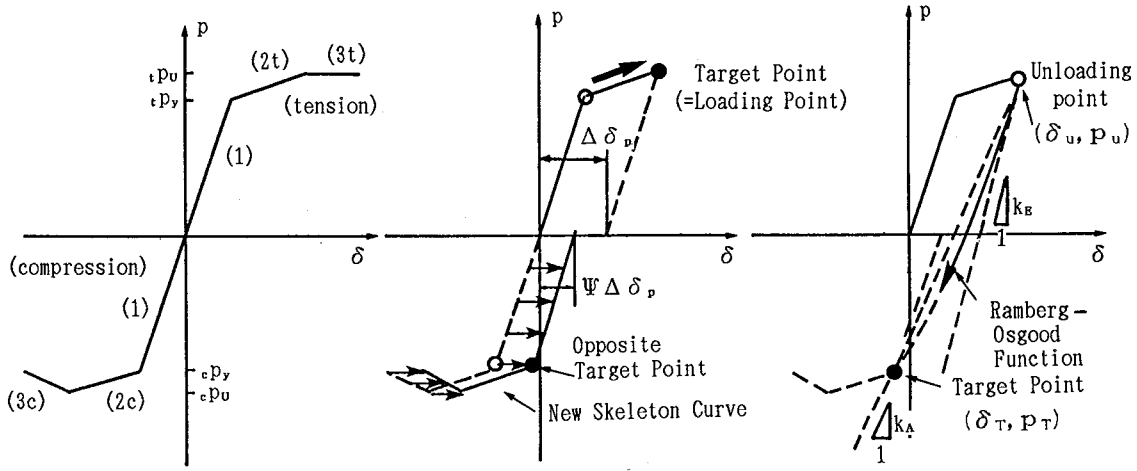

(a) Initial Skeleton Curves (b) Shift of Skeleton Curve (c) Unloading Path

Fig.4 Hysteresis Rule for Bar-Springs

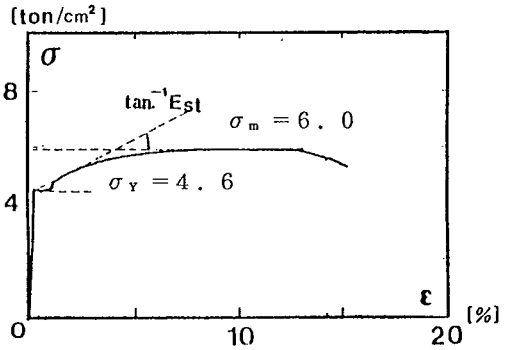

Fig. 5 Typical Stress-Strain Curve of Steel Material Used for Flange Plates

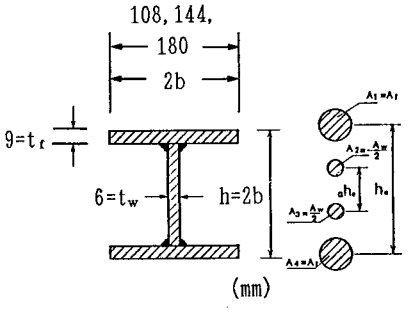

Fig. 6 Four-bar Model for H-shaped Cross-section Tested

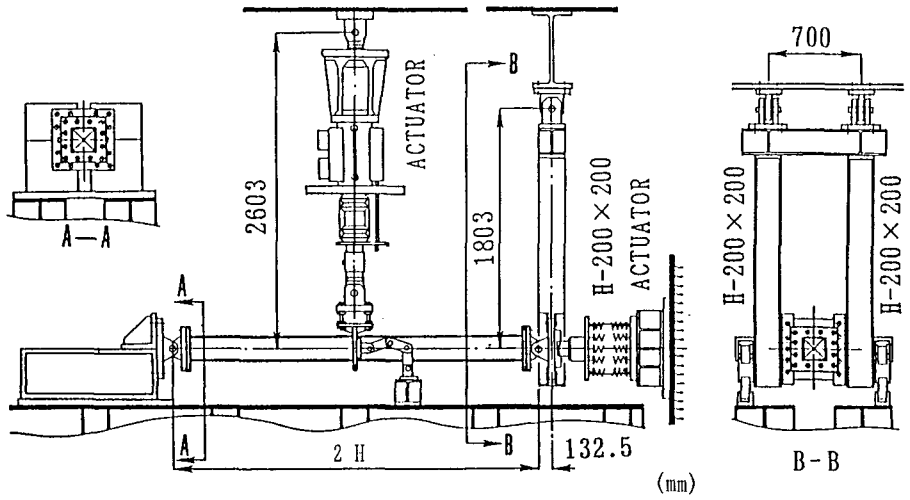

Fig. 7 Test Setup

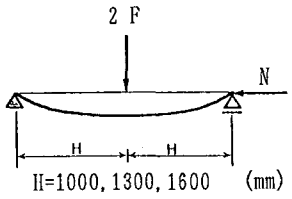

(a) Loaing Test

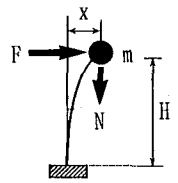

(b) Vibrational System Analyzed in On-line Tests

Fig. 8 Test Schema

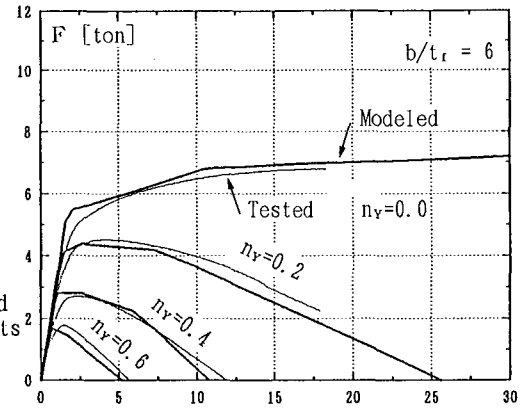

(a) $b/t_f = 6$

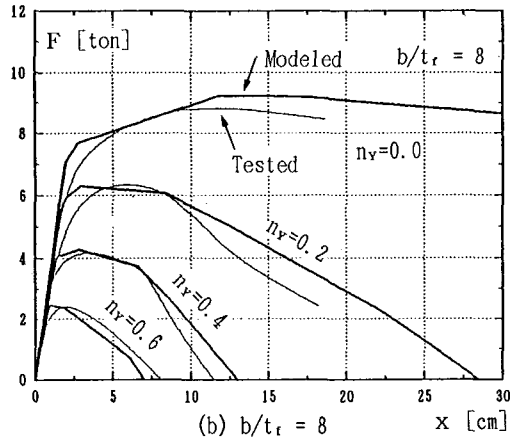

(b) $b/t_f = 8$

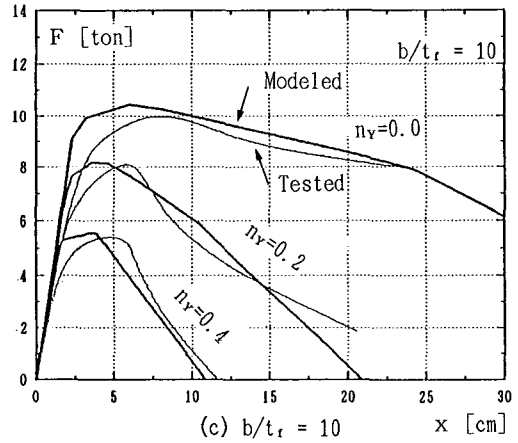

(c) $b/t_f = 10$

Fig. 9 Load deflection Curves — Tested and Modeled
(n_Y : Ratio of Applied Axial Load(N) to Yield Axial Load(N_Y))

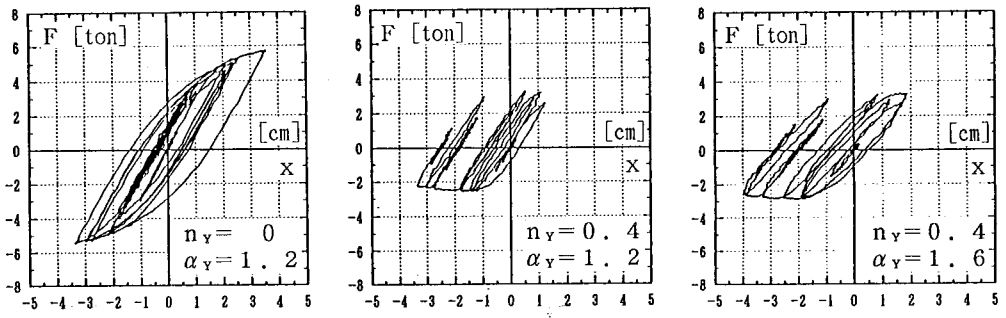

(a) On-line Tests

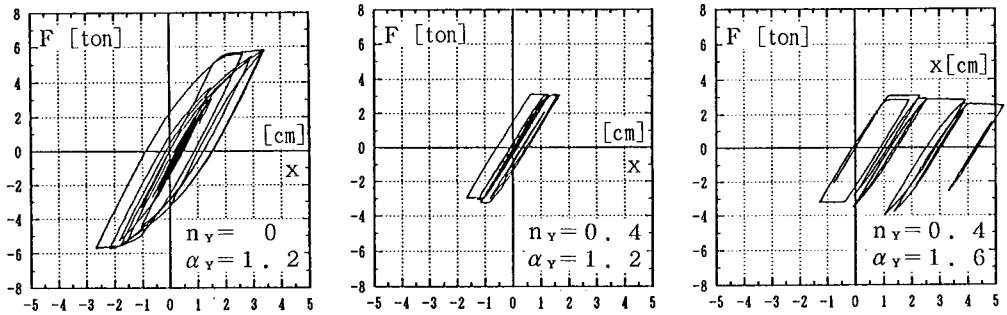

(b) Computed

Fig. 10 Responses to El Centro NS, 1940 (b/t_f=6)

(α_Y : Ratio of Input Peak Acceleration $\ddot{y}$max to Yiel Acceleration (F_Y/m))

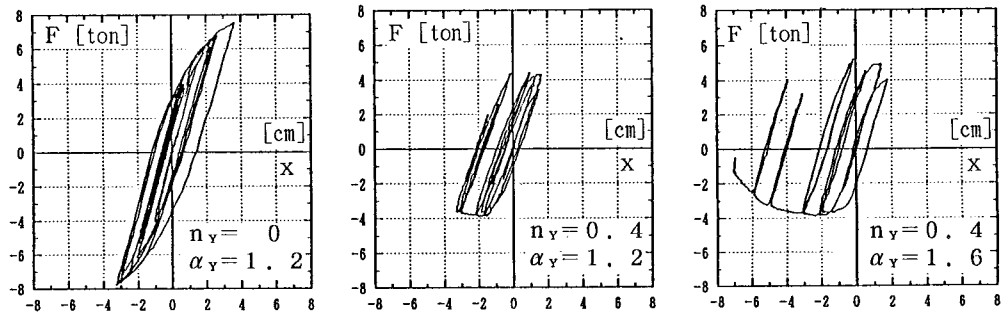

(a) On-line Tests

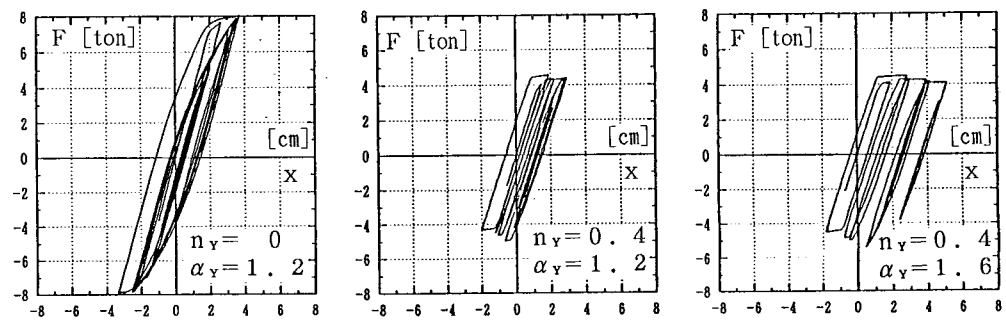

(b) Computed

Fig. 11 Responses to El Centro NS, 1940 (b/t_f=8)

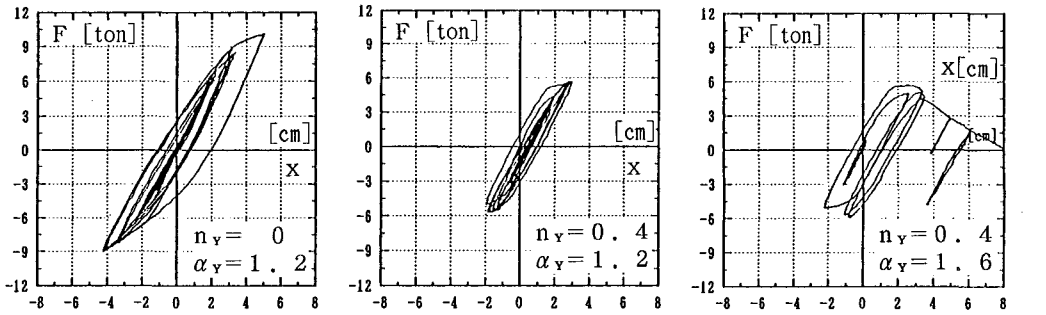

(a) On-line Tests

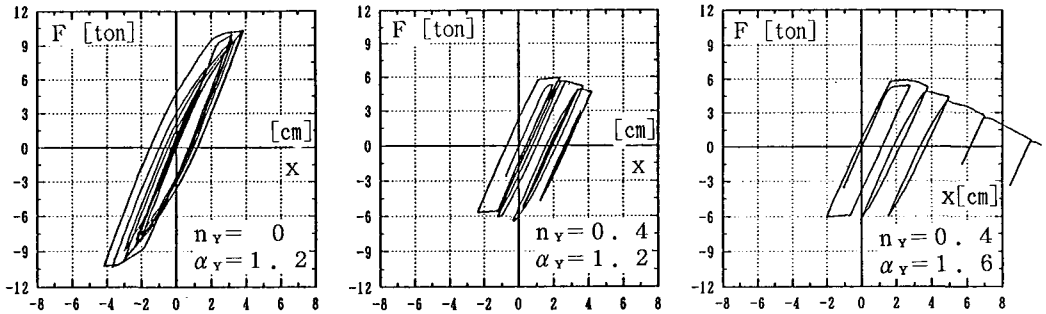

(b) Computed

Fig. 12 Responses to El Centro NS, 1940 (b/t_f=10)

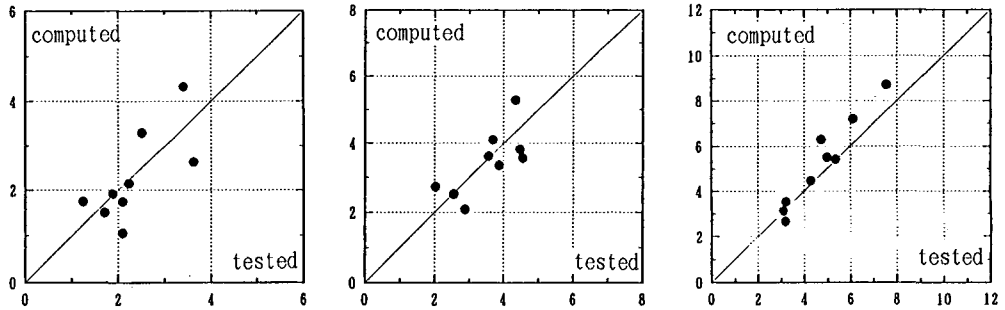

(a) Peak Displacement Normalized by x_Y

(b) Displacement Range Normalized by x_Y

(c) Energy Absorption Normalized by $F_Y x_Y$

($x_Y=M_{pc}H/3EI$, F_Y: M_{pc}/H, M_{pc}: Full-plastic Moment under Axial Load)

Fig. 13 Correlation of Response quantities ---- Tested and Computed